Fluid flow characterisation in randomly packed microscale porous beds with different sphere sizes using micro-particle image velocimetry

Xianke Lu[a], Yuyuan Zhao[a], David J.C. Dennis[a,*]

[a]*School of Engineering, University of Liverpool, Liverpool L69 3GH, United Kingdom*

Abstract

An experimental study using pressure-drop and μ-PIV measurements was undertaken to better understand the fluid flow characteristics in different flow regimes within randomly packed microscale porous beds with different sized spheres. Three sintered glass samples were made with glass spheres having a mean diameter of 170 μm, 430 μm and 710 μm by slightly sintering them between two glass slides, forming a sample with a sandwich structure. Four different regimes, pre-Darcy, Darcy, Forchheimer and turbulent were identified in each sintered glass sample using the pressure-drop measurements. The permeability increases with glass sphere size and so does the Reynolds number corresponding to each flow regime boundary. It was found that for a given Re, the pressure drop in the sample with 170 μm diameter spheres can be ten times higher than the pressure drop in the sample with 710 μm diameter spheres. Four different pore geometries were identified to be the focus of the measurement zones of the μ-PIV, which were taken across a range of Re spanning all the flow regimes identified in the pressure-drop measurements. The non-dimensional time-averaged velocity distribution was found to be similar in each flow regime for the samples with 170 μm and 430 μm diameter spheres, whereas it changed dramatically for the sample with 710 μm diameter spheres. In general the velocity profiles through the channels within the porous media were found to be near-parabolic, especially in the Darcy and Forchheimer regimes, but in the turbulent regime inertial effects such as localised jets were observed. Detailed observational and statistical analysis of the velocity distributions highlights their very strong dependency on the local geometry with highly localised regions of flow apparently in a different flow regime to that of the bulk flow. However, the global average of the fluctuations throughout the measurement zone does align well with the pressure drop measurements.

Keywords: porous media, microscale, fluid flow, micro particle image velocimetry

---

*Corresponding author
  Email address:* `djcd@liverpool.ac.uk` (David J.C. Dennis)

1. Introduction

Fluid flow through porous media is attracting extensive attention due to its broad range of applications in science and industry. The application of fluid flow through porous materials can be found in many fields such as geothermal systems, oil extraction, transpiration cooling, ground water pollution, storing of nuclear waste, catalytic convertors, filters and chemical reactors [1, 2, 3, 4, 5, 6]. Some porous media exist in natural materials, (e.g. rock and sand) and some are man-made (e.g. packed spheres and metal, graphite, ceramic and polymetric foams) [7]. Typically, these porous media contain high surface area per unit volume and tortuous channels [8, 9]. These unique structure characteristics make the flow through porous media very complex, but understanding the flow behaviour is critical for scientific and practical applications.

The complexity of fluid flow through porous media stems mainly from the obstruction of the solid structure in the path of the flow. Fluid has to travel through a winding and tortuous flow channels to pass through the random porous structure [10, 11]. Therefore, the pressure drop in porous media is much higher than an open-area flow (e.g. a straight channel or pipe). In addition, the critical Reynolds number of transition from laminar flow to turbulent flow is difficult to predict, and the relationship between pressure gradient and flow rate may be different under the same flow regime due to the different interactions between fluid and solid phases [12].

For single phase Newtonian fluid flow through porous media, the volumetric flow rate is proportional to the negative of the pressure gradient at sufficiently low flow rate. Darcy [13] first discovered this phenomenon and proposed a linear relationship to describe it. This relationship, named Darcy's law, is $-\Delta P/L = \mu V/K$, where V is the Darcian velocity (equal to the volumetric flow rate divided by the bed cross-sectional area normal to the bulk flow direction), μ is the viscosity of the fluid, and K is the permeability of the media (a measure of the ability of a porous material to allow fluids to pass through it, the value of which depends strongly on the porosity, channel structure and surface roughness). The regime where flow follows Darcy's law is called the Darcy regime. In this regime, the interstitial fluid is dominated by viscous forces from the solid matrix and it shows a linear relationship between pressure gradient and flow rate. As the Reynolds number gradually increases, non-linearity appears in the velocity-pressure gradient relationship. This non-linear relationship is due to the increasing role of the inertial forces. Forchheimer [14] added the contribution of inertial force on the fluid flow and proposed a new relationship. This relationship, called the Forchheimer-extended Darcy equation, is given in equation 1,

$$-\frac{\Delta P}{L} = \frac{\mu V}{K} + \rho C V^2,\tag{1}$$

where ρ is the density of fluid and C is the drag force coefficient (the value of which also depends on the internal structure of the porous media). In this

2

non-linear flow regime both viscous and inertial forces are significant. As the Reynolds number continues to increase, the inertial force gradually increases until it dominates. However, the onsets of the linear and non-linear flow regimes cannot be predicted according to present knowledge, because they depend strongly on the pore structure.

Several efforts have been made towards understanding the different flow regimes in porous media [15, 16, 17, 18]. Dybbs and Edward [19] employed laser anemometry and flow visualization techniques to study the flow behaviours in porous media. Four flow regimes, named as Darcy flow regime, inertial flow regime, unsteady laminar flow regime and turbulent flow regime were identified, and the general flow regime boundaries (critical Reynolds numbers) were also provided in their study. Fand et al. [20] conducted an experiment investigating pressure drop of water flow through various packed beds. Packed beds made from uniform sphere (2, 3, and 4 mm in diameter) and mixed spheres (2.8, 3.3 and 3.7 mm in average diameter) were used in their experiments. Three flow regimes were identified from the reduced pressure drop-Reynolds number curve. Furthermore, by using the sphere diameter based Reynolds number, they found that the flow regime boundaries of different packed beds were identical. Kececioglu and Jiang [21] reported the limited quantitative information on the criteria employed in marking the flow regimes for flow through packed beds in the existing literature. They conducted an experiment investigating resistance to flow of water in randomly packed beds made from 3 mm and 6 mm glass spheres. Four distinct flow regimes, identified as pre-Darcy, Darcy, Forchheimer and turbulent were found in their study. Moreover, it was found that the flow regime boundaries are different if marking them by the sphere diameter based Reynolds number, but they are identical if the square root of permeability is employed as the characteristic length in Reynolds number.

Partha et al. [22] experimentally and numerically studied the single phase flow through different types (homogeneous and mixed isotropic) of porous media and made the conclusion that the microscopic inertial effect is the governing factor for the transition from the Darcy to the non-Darcy flow regime. Li et al. [23] experimentally investigated the effect of particle size on flow regime by driving fluid through a sand column with five different particle sizes ranging from 1 mm to 3 mm. Both pre-Darcy flow and post Darcy flow were identified but the linear flow regime was not identified. Van Lopik [24] studied the effect of the uniformity of granules on the Forchheimer parameter using equal size sand grains and composite sands and found the composite sand increased the parameter significantly. Bagus et al. [25] investigated the effect of pore-scale heterogeneity on non-Darcy flow behaviour by direct flow simulation and found the critical Reynolds number indicating the cessation of the Darcy flow in Estaillades carbonate is two to three orders of magnitude smaller than in Bentheimer sandstone and packed beds.

Numerical simulations have also been conducted to study the flow behaviour in porous media. Fourar et al. [26] examined the non-linear behaviour of single phase flow through 2D and 3D porous media using a unit cell model. The 3D model showed a narrower transition zone than the 2D model. Newman et

3

al. [27] and Chiappina et al. [28] studied the effect of geometry on flow transition using lattice Boltzmann simulations in a 2D and 3D porous medium and the results showed good agreement with the theory. Cloete et al. [29] investigated the effect of an external boundary on the velocity profile as Newtonian fluid passed through a porous domain. Other researchers [30, 31, 32, for example] have studied the fluid flow behaviour at different temperatures in porous media in order to improve the convective heat transfer performance.

Pressure gradient measurements or traditional flow visualization can provide limited information, such as flow regime boundaries, on the flow though porous media. Velocity and stress distributions at the pore scale, and the effects of different structures on these velocity and stress distributions, which are critical in studying flow dynamics in porous media, cannot be obtained from such measurements. By adding seeding particles, the flow behaviour in pore scale can be studied by particle displacement measurement techniques such as laser Doppler velocimetry (LDV) [33, 34, 35, 36], magnetic resonance imaging (MRI) [37, 38, 39, 40], particle tracking velocimetry (PTV) and particle image velocimetry (PIV) [41, 42, 43, 44, 45, 46, 47, 48]. Two-dimensional and three-dimensional velocity distributions at the pore scale have been achieved with these techniques. Most of the previous measurements were conducted based on macroporous media, in which the flow behaviour may be simple and different from microporous media [49]. Recently, advances of μ-PIV make it a powerful tool to visualize the fluid flow behaviour in micro-scale. Lima et al. [50, 51] measured the velocity profile of the citro blood flow in a rectangular and square microchannel using μ-PIV system. Pan et al. [52] studied the flow field of a microchannel filled with micro-beads at very low Reynolds number (less than 0.1) with μ-PIV. Sophie et al. [53] investigated the dynamics of the immiscible two-phase flow in micromodels which is a 2D porous media fabricated by etching onto a silicon plate. Campos Marin et al. [54] investigated how fluid flow conditions modulate cell motion and deposition during perfusion in a 3D scaffold using μ-PTV. Mohammad et al. [55] investigated the interfacial boundary condition and residual trapping of two-phase flow in an artificial porous medium using μ-PIV. However, it is still difficult to obtain high quality experimental data in micro-scale due to the mismatch of refractive index, stack of seed particles, control and measure of slow moving fluid and small pressure differences. Nevertheless, large amount of experimental data can lead to reliable velocity results and these results are significant for understanding porous flow and provide guidance for numerical works[56].

The literature reveals that several experiments using the latest technology to measure the flow field in porous media have been performed. However, none of these studies include a velocity field measurement of the flow through porous media (alongside pressure drop measurements) at conditions covering all the flow regimes. Understanding the different flow behaviours in different regimes is fundamental to our understanding of the flow through porous media and crucially important for the successful application of porous materials in scientific and engineering devices. In this paper, both the flow hydrodynamics and velocity distribution are quantitatively investigated in micro-porous media made
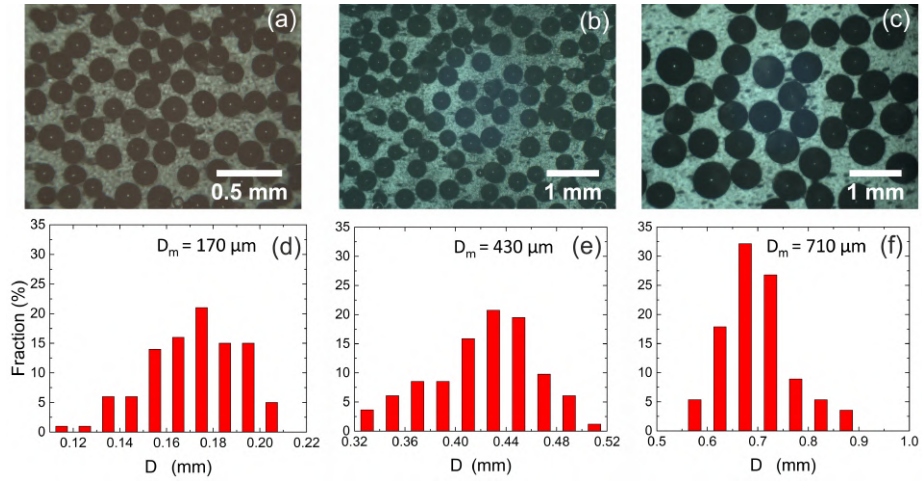
4

Figure 1: Micrographs of the glass spheres with diameter ranges of (a) 100-200 μm, (b) 300-500 μm and (c) 500-900 μm, and the corresponding particle size distributions, (d), (e) and (f), respectively.

from sintered glass spheres using μ-PIV measurements. A special feature of the porous media used in the current study is that they are made of micron-scale glass beads having a diameter range rather than a fixed diameter, which makes the internal channels more distorted and the flow more complex. A flow rate range from the pre-Darcy regime to the turbulent regime was covered in the experiments. The flow regime boundaries are compared (in terms of mean diameter based Reynolds number and permeability based Reynolds number) with the existing data. The effect of sphere diameter on flow regime boundary and permeability is discussed. Four typical pore geometries are identified and the velocity data, velocity distribution and fluctuations of the velocity measured using μ-PIV at the pore scale are described in detail.

2. Experimental

2.1. Preparation of porous samples

Three types of glass spheres (Bound Minerals Ltd, UK) with diameter ranges of 100-200 μm, 300-500 μm and 500-900 μm were used to fabricate the sintered glass samples. The corresponding mean diameters are 170, 430 and 710 μm, respectively. The mean diameter of the glass sphere powder was taken as the Sauter mean diameter [57], which was determined from the mean volume equivalent diameter. Figure 1 shows the micrograph and particle size distributions of the glass spheres. The glass particles are spherical and have a smooth surface. The particle size distributions were obtained by measuring the diameter of each sphere using Image J software.

The sandwich structure samples were made by lightly sintering the glass spheres together between two glass slides, avoiding the use of other components

Table 1: Physical properties of sintered glass samples.

Sample	D (μm)	D_m (μm)	ϵ (%)	α
SG170	100-200	170	34	8.52
SG430	300-500	430	35	3.48
SG710	500-900	710	40	2.11

such as perforated plate or wire mesh to support the packed spheres. In the fabrication process, a glass slide with dimensions of 26 mm × 25 mm × 1 mm, was placed at the bottom of a steel mould with the same cross-sectional area, then the weighed glass beads were poured into the mould, and another glass slide was placed on top. The preform was sintered in two steps and the details can be found in our previous work in [56].

Three sintered glass samples, corresponding to the three glass sphere diameter ranges, were fabricated by the above process. The dimensions of the sintered porous structure, (excluding the thickness of glass slides) are 25 mm × 26 mm × 1.5 mm. The porosity of the sample was measured by direct volume measurement. Table 1 lists the sample details, including glass sphere diameter (D), mean diameter (D_m), porosity (ϵ) and aspect ratio (α). The aspect ratio is the ratio of sample height to spheres diameter, with lower aspect ratios leading to stronger effect of the top and bottom walls on the porosity[58].

2.2. Flow system and image acquisition system

Figure 2 schematically shows the experimental set-up designed for the flow visualization and pressure drop measurements. It mainly includes a flow system and a μ-PIV system. The experimental setup is only briefly described here as it is the same as reference [56]. A syringe pump (Harvard Apparatus, PHD ULTRA) and pressure vessel were used to drive fluid through the porous sample at low and high flow rate, respectively. The working section is a rectangular channel with a sample fixed at a specific position. There are two pressure ports (inlet and outlet side) on the channel connected to a pressure transducer and a window for visualization. A range adjustable pressure transducer (e.g., 3.5 kPa, 22 kPa and 140 kPa, Validyne Engineering, USA) was applied across the sample to obtain accurate pressure drop measurements. The working fluid is water, seeded with 1-micron fluorescent spheres.

The visualization was achieved through a μ-PIV system (Dantec Dynamics, Denmark), which consists of a pulsed Nd:YAG laser (New wave Solo III, Dantec Dynamics, Denmark) with wavelength of 532 nm, a CCD camera (FlowSense series, Dantec Dynamics, Denmark) with resolution of 1600 × 1200 pixels and a microscope (Leica Microsystems Ltd.) with adjustable lens. Lenses with different magnifications were used depending on the particle sizes (pore sizes), as presented in table 2. The smaller numbers in the table are the magnification of the lens and the larger numbers in the brackets are the total magnification of the microscope system. High magnification makes it possible to view the
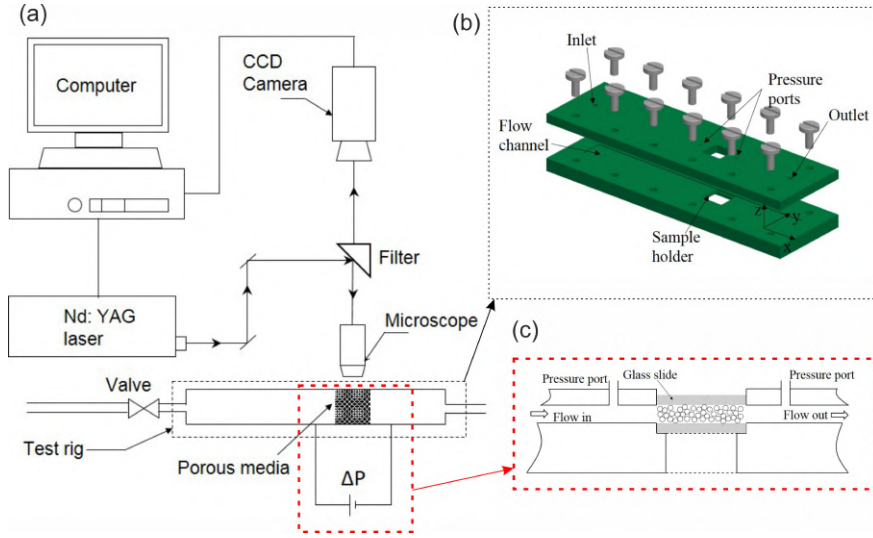
Figure 2: Experimental setup used for micro-PIV and pressure drop measurements (not to scale), (a) Flow system, (b) flow channel (scaled) and (c) test section.

Table 2: Lens and view properties for each sample.

Sample	Magnification	Aperture	DOF (μm)	FOV (mm)
SG170	40 (400)	0.6	1.0	0.54×0.40
SG430	20 (200)	0.4	5.8	1.08×0.81
SG710	10 (100)	0.25	8.5	2.16×1.62

flow at micro-scale, and a short depth of field is utilized to exclude the particles in adjacent layers. However, high magnification also significantly reduces the seed particle density due to the shorter depth of field (DOF) and smaller field of view (FOV). Therefore, more seed particles were added to the fluid at high magnification to obtain an acceptable particle density.

2.3. Measurement procedure

In each experiment, the porous sample was first placed in the test section and then sealed by silicone, leaving 24 hours to dry. The pressure drop measurements and μ-PIV experiments were conducted separately because different flow rate steps were used and the μ-PIV experiments need to be guided by the pressure drop results. Before each measurement, a high flow rate (e.g. 500 ml/min) was applied through the sample for 5 minutes to flush out any air bubbles inside the sample.

For the pressure drop measurement, the flow rate was varied from low to high in steps of 1 ml/min and 10 ml/min in the flow rate ranges of 1-30 ml/min and 30-500 ml/min, respectively. The exact upper flow rate limit depends on
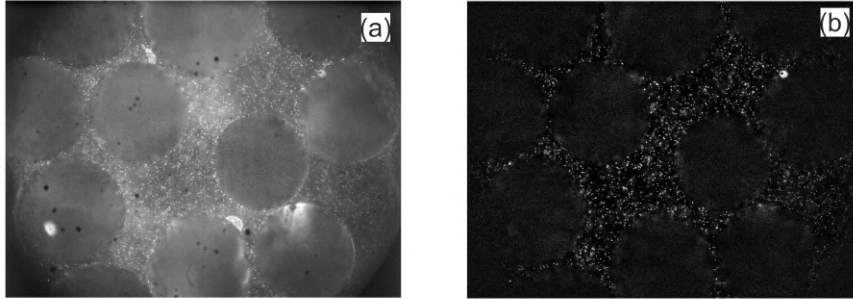
7

Figure 3: (a) A typical raw image acquired from μ-PIV in sample SG710 and (b) background removed image. The magnification of the image is 100 times.

the sample. For each flow rate, 60 seconds was allowed for the flow to reach a steady state before recording the pressure data, the pressure recording lasted about 60 seconds at a sampling rate of 100 Hz and the mean value was used.

The μ-PIV experiment was conducted immediately after the pressure drop measurement. As the FOV of the measurement was significantly smaller than the sample size, one region was selected for PIV in sample SG170 and SG710, and two regions were selected in sample SG430. The flow rate for the μ-PIV measurement was determined according to the pressure drop results. The μ-PIV measurements were conducted on each region at ten different flow rates to ensure that the flow behaviour in each of flow regime could be visualized. 300 pairs of images were acquired at a frequency of 8 Hz at every chosen flow rate for each sample. The time interval between the two frames in each pair ranged from 5 μs to 9000 μs, for the highest to lowest flow rate. DynamicStudio was used to collect images and calculate the velocity field. Each pair of frames was divided into an interrogation area with 32 × 32 pixels, and the velocity was calculated using 50% overlap, resulting in a velocity vector map with 7326 vectors. Figure 3(a) displays one of the typical raw images acquired from sample SG710 at the magnification of 100. Some fluorescent particles attach to the surface of the glass spheres, forming bright spots and reducing the contrast seriously at that area. Therefore, the near wall region was removed from the image in post processing due to high uncertainty. In addition, the blurred image of some fluorescent particles just outside the focal plane are still visible despite the short depth field. The shadow of the glass spheres and blurred particles remained on the image after the background was removed from the raw image, as shown in figure 3(b). This problem was solved by subtracting a threshold value, which depends on the signal to noise ratio, from the processed image.

2.4. Measurement uncertainty

Beyond the typical encountered errors in fluid flow visualization [59], porosity and μ-PIV measurement due to refractive index mismatch are the two main uncertainty in this study.

8

The porosity uncertainties in this experiment were due to errors in measurements of the mass of the glass slides and the porous sample, and the dimensions of the samples. According to the method of Kline and McClintock [60], the uncertainty of the porosity defined in this study can be calculated as in equation 2,

$$\frac{\Delta\epsilon}{\epsilon} = \sqrt{\left(\frac{\Delta m_{gs}}{m_{ps} - m_{gs}}\right)^2 + \left(\frac{\Delta m_{ps}}{m_{ps} - m_{gs}}\right)^2 + \left(\frac{\Delta l}{l}\right)^2 + \left(\frac{\Delta w}{w}\right)^2 + \left(\frac{\Delta h}{h}\right)^2},$$
(2)

where m_{gs} and m_{ps} are mass of glass slides and porous sample respectively, l, w and h are the length, width and height of sample. The error of the balance and calliper measurements was 0.01 g and 0.01 mm. The typical mass of a slide and a sample are about 2.8 g and 4 g. With each factor determined, the total error of porosity was estimated to be 1.21%.

The μ-PIV measurement uncertainty was calculated according to the method outlined by Meinhart et al. [61]. The diameter of the seed particle appear on the CCD chip can be calculated according to equation 3,

$$d_e = \sqrt{M^2 d_p^2 + d_s^2},$$
(3)

where d_p is the seeding particle size (1 μm in this study), M is the magnification of the microscope. d_s is the diameter of the diffraction-limited point and is given by equation 4,

$$d_s = 2.44 M \frac{\lambda}{2N_A},$$
(4)

where λ is the wavelength of the light and N_A is the numerical aperture of the lens. For the 40$\times$ objective lens with $N_A = 0.6$, the size that the particles appear on the CCD chip is about 58.8 μm. The pixel size of the CCD chip is 7.4 μm, allowing the particle to be resolved by 3-4 pixels. The measurement uncertainty in one direction is yielded by $\sigma_x = d_e/10M$ [61]. For a typical displacement of a particle between two frames, e.g. at velocity of 0.57mm/s and time interval of 5000 μs, the typical uncertainty was evaluated to be 5.2%.

3. Bulk flow measurements

3.1. Pressure drop

The relationship between the sample length-normalized pressure drop and the particle size based Reynolds number for sintered glass samples with different mean diameter are shown in figure 4. The particle size based Re was defined as in equation 5,

$$Re = \frac{\rho V D_m}{\mu},$$
(5)

where ρ is the density of water, μ is the viscosity of water, D_m is the mean diameter and V is Darcian velocity. It is observed that, for a given Reynolds
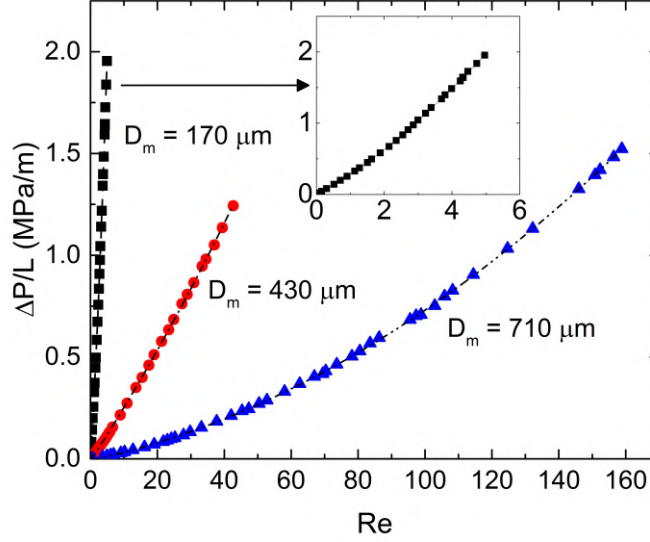
Figure 4: Relationship between the pressure drop per unit length versus Reynolds number across the porous bed with different particle sizes. The inset magnifies the plot for $D_m = 170\mu$m.

number, the pressure drop in the sample fabricated from smaller particles is much higher than that for those fabricated from larger particles. This is caused by the lower porosity and greater resistance from the increased surface area and tortuosity in the small particle samples. The linear relationship between pressure drop and Re is too narrow to be identified in this figure, but the nonlinear relationship between them fits a quadratic function well.

3.2. Flow regimes

The Forchheimer-extended Darcy equation (equation 1) can be rewritten in other form to express the relationship between reduced pressure drop ($\Delta P/LV$) and Re. It is shown in equation 6,

$$-\frac{\Delta P}{LV} = \mu \left(\frac{1}{K} + \frac{C}{D_m} Re \right). \tag{6}$$

Different flow regimes can be identified by observing the change in the slope of the $\Delta P/LV$ vs Re plot, i.e. the value of the C. Figure 5 is the plot of the reduced pressure drop versus Re. Four different flow regimes: (i) pre-Darcy, (ii) Darcy, (iii) Forchheimer and (iv) turbulent, which are corresponding to $C > 0$, $C = 0$, $C > 0$ (higher magnitude) and $C > 0$ (lower magnitude), respectively, were identified. The flow behaviour is similar to that measured in porous media made using a space-holder method [56].

The nature of the flow in the pre-Darcy regime is not clearly understood due to experimental difficulties in accurately measuring the rather small flow
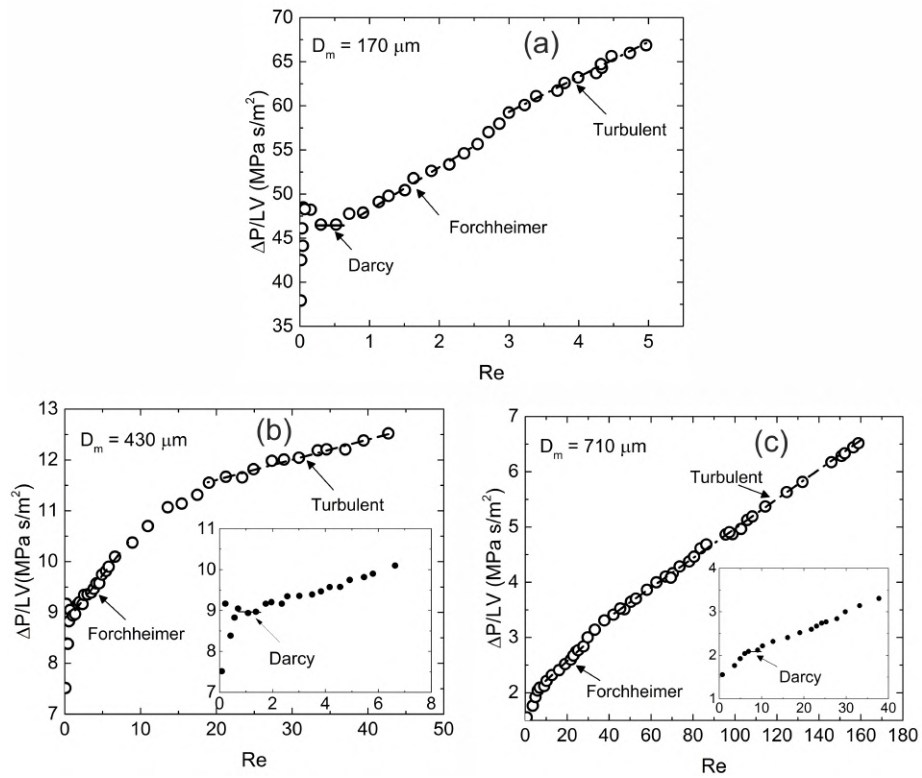
10

Figure 5: Reduced pressure drop versus Reynolds number for (a) $D_m = 170\mu$m, (b) $D_m = 430\mu$m and (c) $D_m = 710\mu$m. The inset plots in (b) and (c) are a magnification of the low Reynolds number range and have the same axes as the main plots.
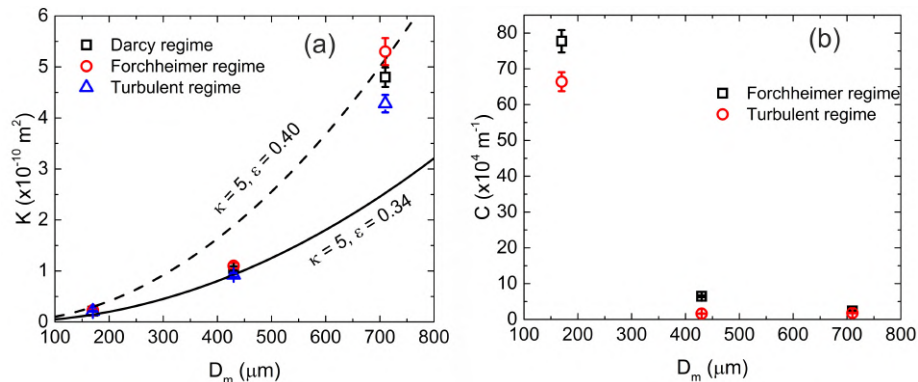
Figure 6: Relationships of (a) permeability (K) and (b) form drag coefficient (C) with mean particle size in the three sintered glass samples.

rates and pressure drops associated with it, although some hypotheses have been made by previous researchers (e.g. [62, 56]) to explain the phenomena in this regime. The Darcy regime exists only at low flow rates and spans a narrow flow-rate range. Since pressure drop in this regime is only produced by the viscous force from the inner surfaces of the solid phase in the sintered glass sample, the characteristics of the flow reflects the actual geometry of the internal structure. In Forchheimer and turbulent regimes, both the viscous forces and the inertial force play an important role. The effect of the near-wall layers becomes much more significant compare to that in the Darcy regime where they are developed [19].

3.3. Effect of particle size

The pressure drop-Re relationship in both the Forchheimer regime and the turbulent regime in sintered glass samples can be described by the Forchheimer-extended Darcy equation, but with different parameter (permeability and form drag coefficient) values. Figure 6 shows estimates of the permeability (K) and form drag coefficient (C) for three sintered glass samples. The permeability and form drag coefficient values for each regime were obtained by fitting the experimental data to corresponding equations, e.g. Darcy regime fitted with the Darcy equation and the Forchheimer and turbulent regimes fitted with the Forchheimer-extended Darcy equation. Figure 6 shows that increasing the particle size results in a significant increase in permeability and a significant decrease in form drag coefficient. The lower fluid resistance in a sample with large particle size is due to lower surface area impeding the fluid flow and a relative high porosity, leading to a less tortuous flow path.

The experimental permeability is also compared with the value predicted from the semi-empirical expression given in equation 7 [21] and they are consistent

$$K = \frac{\epsilon^3}{s_v^2 \kappa (1-\epsilon)^2} = \frac{D_m^2 \epsilon^3}{36\kappa (1-\epsilon)^2}. \tag{7}$$

12

In equation 7, ϵ is the porosity, s_v is the surface area per unit volume of the particles and κ is a dimensionless constant known as Kozeny-Carman constant, the value of which is recommended as $\kappa = 5$ for smooth spherical particles [63]. The predicted permeability for porous media with porosity of 0.34 and 0.40 was plotted by a solid and dashed line in figure 6. The experimental data show good agreement with equation 7 despite the sintered glass samples having different aspect ratios.

Table 3 compares the flow regime boundaries identified for our sintered glass samples with several datasets available in the literature. The flow regime boundaries in terms of both mean particle diameter based Reynolds number and permeability based Reynolds number (in brackets) are shown. The permeability based Reynolds number is defined as $Re' = \rho V_i \sqrt{K/\epsilon}/\mu$, where V_i is the interstitial velocity, equalling to the Darcian velocity divided by porosity, K is the permeability calculated in the Darcy regime and ϵ is the porosity. Table 3 shows that neither the particle size based onset Reynolds numbers, nor the permeability based onset Reynolds numbers are the same for all the samples in this study. However, the general trend for all the porous media is that the onset Re for each flow regime increases with particle size.

Table 3: Flow regime boundaries of current and previous studies. Values in brackets are permeability based Reynolds number.

Reference	Diameter	Pre-Darcy	Darcy	Forchheimer	Turbulent
Current study	170 μm	< 0.2	0.2-0.5	0.9-2.5	> 3.0
		(< 0.03)	(0.03-0.07)	(0.12-0.34)	(>0.40)
	430 μm	< 0.7	0.8-1.3	1.7-10.9	>19
		(< 0.08)	(0.09-0.16)	(0.20-1.27)	(> 2.22)
	710 μm	< 6.0	6.5 - 9.0	12-27	> 42
		(< 0.76)	(0.8-1.2)	(1.5-3.5)	(> 5.4)
Fand et al. [20]	2-4 mm	NA	< 2.3	5.0-80	> 120
			(< 0.26)	(0.57-9.00)	(> 13.5)
Kececioglu et al. [21]	3 mm	< 0.3	0.3-0.7	1.6-10	> 13
		(< 0.062)	(0.062-0.120)	(0.34-2.30)	(> 3.4)
	6 mm	< 0.6	0.6-1.0	3.0-21	> 25
		(< 0.062)	(0.062-0.120)	(0.34-2.30)	(> 3.4)

Figure 7 plots the variation of Reynolds number for the onset of each flow regime with mean particle size of the porous media. The onset Reynolds numbers for the transition to Darcy, Darcy, transition to Forchheimer, Forchheimer, transition to turbulent, and turbulent are designated as Re_D, Re_{TF}, Re_F, Re_{TT} and Re_T, respectively. The Reynolds number ranges for the pre-Darcy, Darcy, transition to Forchherimer, Forchheimer, transition to turbulent and turbulent regimes are therefore: $Re < Re_D$, $Re_D < Re < Re_{TF}$, $Re_{TF} < Re < Re_F$, $Re_F < Re < Re_{TT}$, $Re_{TT} < Re < Re_T$ and $Re > Re_T$, respectively. Figure 7 shows that the onset Re for each regime increases dramatically with particle size. For example, turbulent flow starts at $Re_T = 3.0$ in the sample with a mean particle size of 170 μm, while it starts at $Re_T = 42$ in the sample with a mean particle size of 710 μm. The Re range for each regime becomes wider with increasing particle size, especially so for the Forchheimer regime.

4. Flow velocity measurements

A Cartesian right-hand coordinate with $x =$ longitudinal, $y =$ transverse, $z =$ bed normal, with the longitudinal direction being parallel to the bulk flow direction, is used to presented all velocity measurements. The velocity components in x and y directions are denoted with u, v and the velocity component in z direction is not measured. The local measured velocity magnitude is $U = \sqrt{u^2 + v^2}$ and the time-averaged local velocity magnitude is represented by $\bar{U}$.

4.1. Instantaneous velocity distribution

Figure 8 displays four different local structures and the corresponding instantaneous velocity distribution at a Reynolds number in the Darcy regime. D170 and D710 were taken from sample SG170 and SG710, and D430a and D430b were taken from sample SG430. All of these regions were located around the centre of the sample, at an approximately equivalent distance from the entrance and exit of the porous media.

Each of the geometry has a unique structure and therefore a unique flow field. D170 is a flow around two spheres with different diameters. Most of the fluid passes this geometry through the relatively wide channel in the lower half of the FOV, resulting in a very asymmetric flow pattern around the two spheres. D430a is a situation where a high velocity flow impinges onto a solid sphere, resulting in a stagnation region and a quite symmetric flow pattern around the sphere. D430b is a flow crossing over a junction of size $\sim D_m$ where fluid enters the junction through four inlets and exits through two outlets. Also worth noting is that there is a glass sphere just below the focus plane in this junction area, visible in figure 8(e). D710 is a repeated jet-like flow with high velocity flow entering into the voids from small gaps. The development of flow from the Darcy to turbulent regime, and the velocity fluctuations in these areas, are discussed in the following sections.
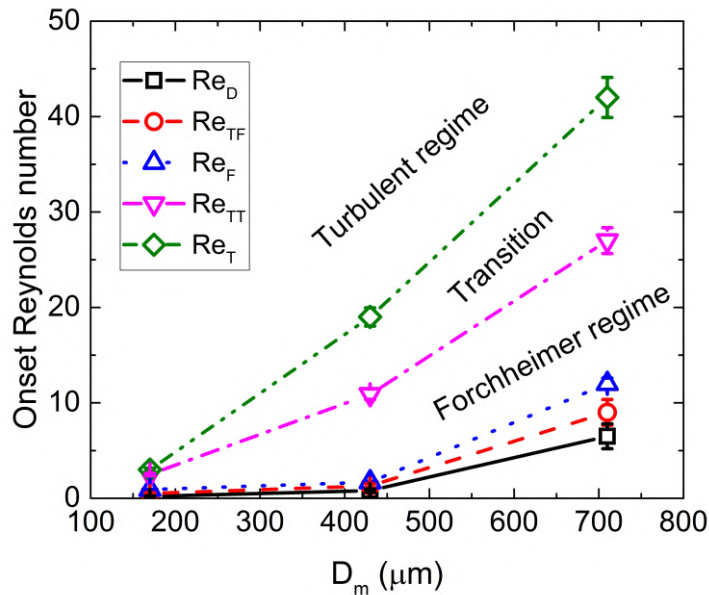
15

Figure 7: Relationship between onset Reynolds numbers and mean particle size of the porous media.

4.2. Time-averaged velocity distribution

The time-averaged velocity distribution from the pre-Darcy to the turbulent regime was studied in order to gain an insight into the details of the flow behaviour in each of the unique porous structures in each flow regime. The time-averaged flow behaviour is qualitatively similar for all Re tested in some of the samples (e.g. D170, D430a and D430b) whilst the behaviour of the flow can be very different at different Re in other samples (e.g. D710). Therefore, the flow behaviours in D170, D430a and D430b are discussed briefly and the flow behaviour in D710 is discussed in more detail.

Figure 9 displays the contour plots of the time-averaged velocity magnitude normalized by the Darcian velocity at a specific Re, alongside velocity profiles along reference lines at various Re for D170, D430a, and D430b. (Note that the ends of reference lines do not reach the solid walls to avoid the high uncertainty of μ-PIV in the near-wall region. Therefore, the velocities at the ends of reference lines is not zero.) The contour plots of the non-dimensional velocity distribution are similar in each flow regime for these three regions, which is shown in figure 10 for D170. We therefore do not focus much on these samples, but on the samples that show significant variation at different Re.

Figure 9 shows that the local structure of D170 and D430a is similar, but the velocity distribution at the pore scale (contour plots) is different. The velocity is asymmetrically distributed in D170 and symmetrically distributed in D430a. This can be attributed to the symmetry of the geometry, with D170 appearing
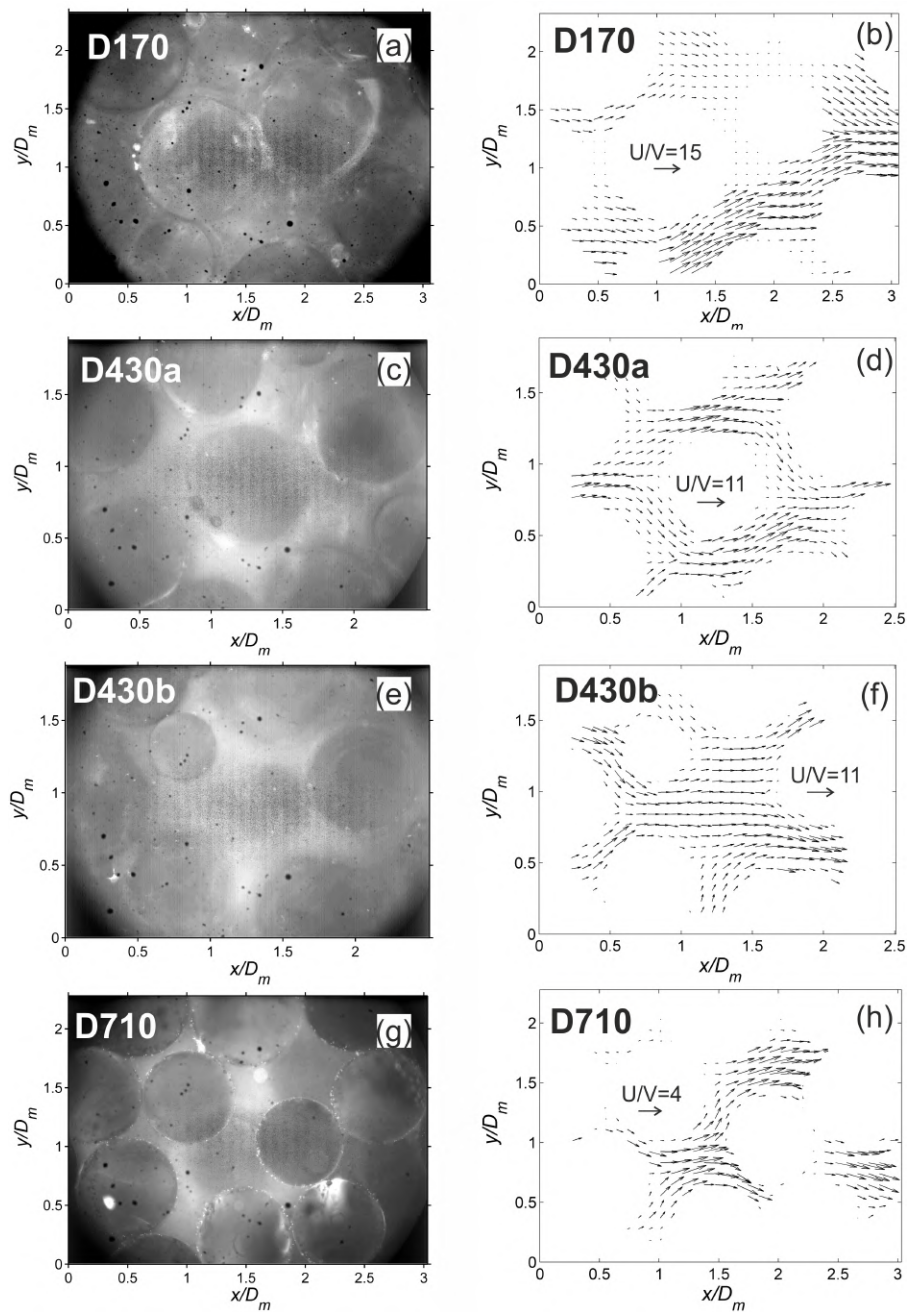
Figure 8: Local structure of sample (a) $D_m = 170\mu$m, (c) and (e) $D_m = 430\mu$m, and (g) $D_m = 710\mu$m; (b), (d), (f) and (h) are the corresponding instantaneous velocity distributions in the Darcy regime (Re of 0.39, 1.1, 1.1 and 6.9 respectively).
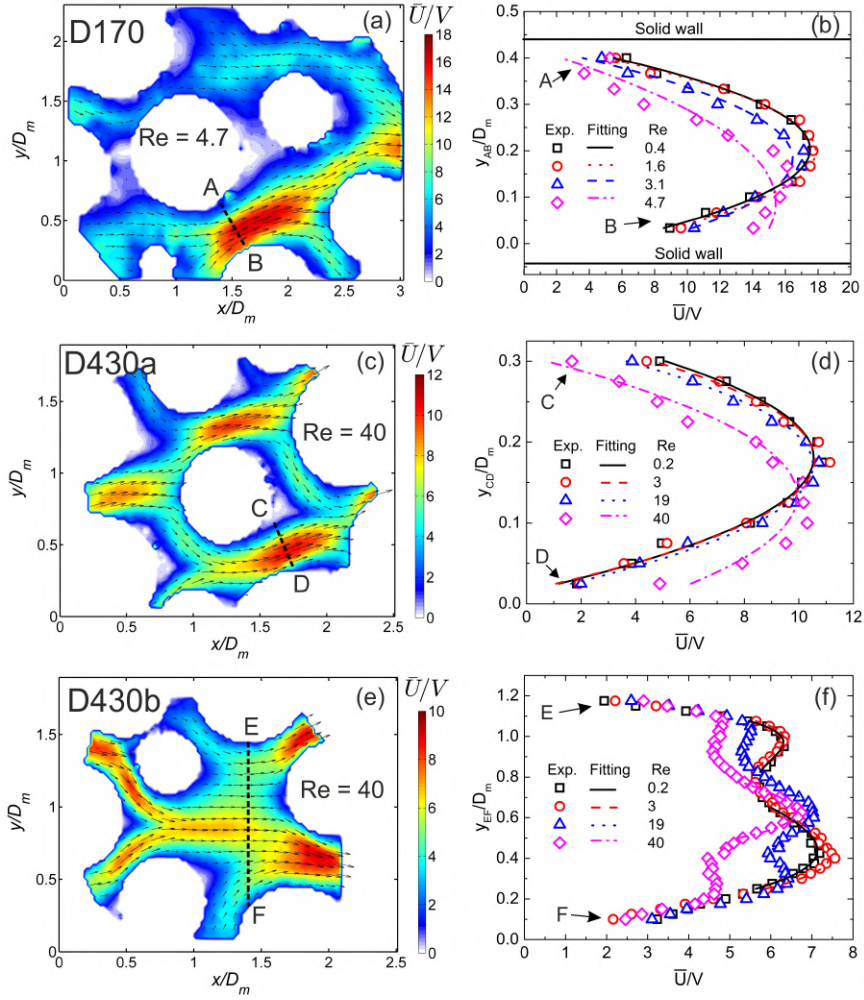
17

Figure 9: Time-averaged non-dimensional velocity distribution in sample (a) $D_m = 170\mu$m (D170), (c) $D_m = 430\mu$m (D430a) and (e) $D_m = 430\mu$m (D430b), and (b), (d) and (f) are the corresponding velocity profiles at different Re along the reference lines of AB, CD and EF, where y_{AB}, y_{CD} and y_{EF}, are the absolute lengths of the reference lines. The colour in the contour plots represents the time-averaged velocity magnitude normalized by the Darcian velocity. The solid glass beads were set to white as only noise exists in these regions.
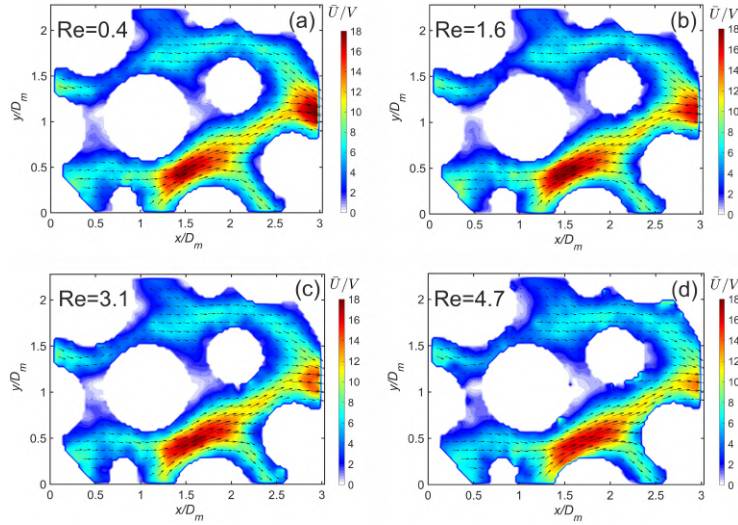
18

Figure 10: Time-averaged non-dimensional velocity distribution in sample $D_m = 170\mu$m (D170) at (a) Darcy regime, (b) Forchheimer regime, (c) and (d) turbulent regime.

to have two flow paths with significantly different widths, whereas in D430a both flow paths are of similar widths. We note, however, that as we are taking measurements in a plane, we cannot comment with certainty on the flow areas
400 as we do not know their depths in the out-of-plane direction. The velocity profiles along the reference lines AB and CD are also similar, both showing a parabolic shape at all Reynolds numbers and a downwards skew (towards B at $Re = 4.7$ in D170, and towards D at $Re = 40$ in D430a) in the turbulent regime. In D430b, the normalised velocity magnitude decreases in the near-wall
405 regions (near E and F) and increases in the central region ($y_{EF} \approx 0.6$) when the flow transitions from the Darcy-Forchheimer regime ($Re = 0.2$ and 3) to the turbulent regime ($Re = 19$ and 40). This can be attributed to the jetting effect of the flow through the small entrance gap into the centre of the larger region where EF is located. At high Re there is sufficient inertia for this jet to exist
410 and penetrate deep into this region (reaching the EF plane), whereas at low Re, with negligible inertia, the jet does not form. The velocity profile shows a parabolic shape in some areas even in this complex region, as displayed by the fitting lines in figure 9(f).

Figure 11 displays the development of normalised time-averaged velocity
415 with Reynolds number (i.e. for different flow regimes) at the pore scale in D710. We mainly focus on the lower left part of the flow field, which has been marked with two inlets (inlet 1 and inlet 2), two outlets (outlet 1 and outlet 2) and a reference line (GH) in the junction. The velocity profile along the reference line of GH is shown in figure 12.

420 Figure 11 shows that the velocity distribution is similar for all Re before the turbulent regime ($Re = 5$ and 26), but changes significantly in turbulent
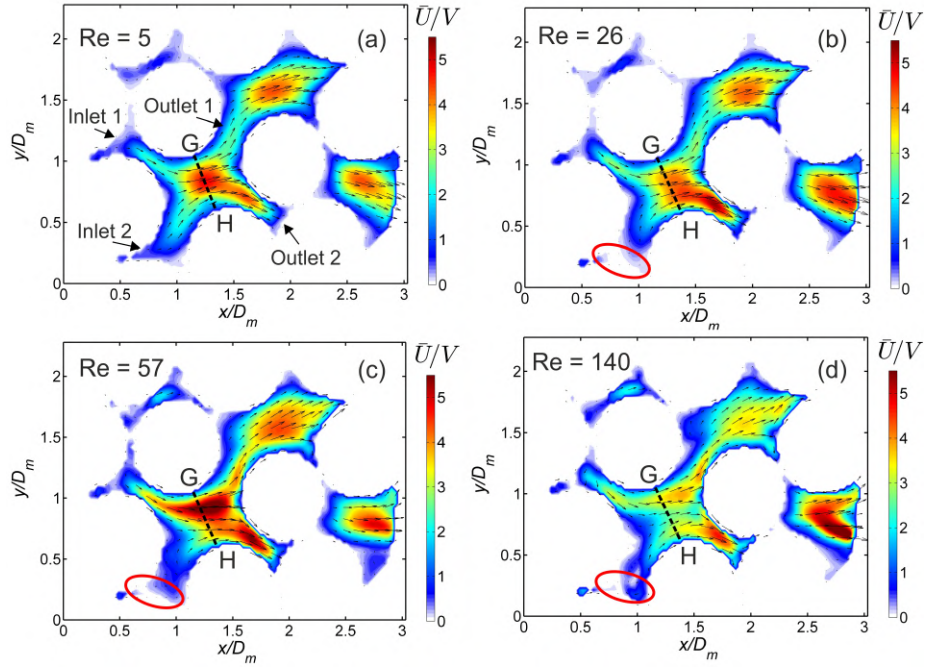
Figure 11: Time-averaged non-dimensional velocity distribution in sample $D_m = 710\mu$m (D710) at (a) pre-Darcy regime, (b) Forchheimer regime, (c) and (d) turbulent regime, presented in the same form as figure 9
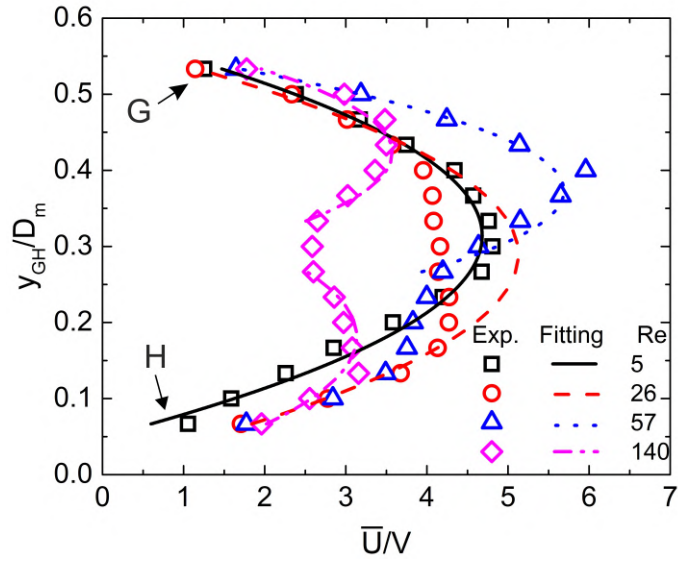

Figure 12: Velocity profile at different flow regimes along the reference line GH in figure 11. y_{GH} is the absolute lenght of the reference line.

regime ($Re = 57$ and 140). In the pre-Darcy regime ($Re = 5$), the velocity magnitude in the two inlets is similar, but it is significantly higher in outlet 2 than in outlet 1. This is probably because outlet 2 is more coincident with the bulk flow direction in the channel and thus is a less tortuous flow path than outlet 1. The velocity profile along line GH is a typical parabolic shape in this regime (see figure 12). In the Forchheimer regime ($Re = 26$), there is an area (marked by a red circle in figure 11) in which the velocity is close to zero in the wake region of a glass sphere located near inlet 2. The result of this is that the flow becomes even more skewed towards outlet 2 than it was in the Darcy regime, which also can be seen from the velocity profile along GH in figure 12. In addition, this profile highlights that the velocity in the centre of the junction is almost uniform, similar to a plug flow.

In the turbulent regime the velocity distribution differs from previous regimes and also changes significantly as the Reynolds number changes from $Re = 57$ to 140 (both turbulent Re). The development of the velocity distribution in the turbulent regime can be divided into three phases: initial phase, transition phase and stable phase. In the initial phase ($Re = 57$), the velocity in the junction is higher near the G wall as the flow enters rapidly from inlet 1 and heads directly towards outlet 1. Near the H wall the flow enters at a much lower velocity from inlet 2, but accelerates as it merges with the flow from inlet 1 and the velocity is also high through outlet 2. The velocity profile along the line GH in figure 12 ($Re = 57$) displays this asymmetric feature, with the velocity profile near point G still showing a parabolic shape, but a quite different shape near H. In addition, the normalized velocity magnitude through the inlet 1 and outlet 1 is increased compared to previous regimes (darker red). These effects can be attributed to the increasing significance of inertia and its role in beginning to keep the two inlet streams distinct. In the Reynolds number range 57 to 140, the velocity near point G gradually decreases until another state is reached where the normalized velocity magnitude is closer to uniform in the junction area. In this phase ($Re = 140$), recirculation is observed near inlet 2 area (red circle). The velocity profile along line GH for $Re = 140$ in figure 12 shows that the flow splits quite evenly between outlet 1 and 2, with two distinct (but similar in magnitude) parabolic velocity profiles near walls G and H and a relatively small dip in the central region. This demonstrates the increasing role of inertia in maintaining two virtually distinct streams through the entire area.

4.3. Statistical analysis of velocity magnitude

A statistical analysis of the velocity field at different Re in measurement zones D170, D430a, D430b and D710 was conducted by examining the probability distribution of the longitudinal (u) and transverse (v) velocity components normalized by the Darcian velocity as shown in figure 13. In all cases the longitudinal velocity component shows a strong skewness towards the positive or bulk downstream direction (left to right in all our images) and the transverse velocity shows a largely symmetrical distribution about $v/V = 0$, which is consistent with expectations [58, 64, 65]. Due to the large surface area in the porous structure, a large proportion of the flow is in the vicinity of a wall, thus the modal

21

velocity tends to be a low value of u/V. This can be confirmed by comparing figure 13 with the contour maps in figures 9 and 11 where it can be seen that the velocity magnitude corresponding to the peak in the pdf is located near the solid walls in the contour maps. The exception to this is D430b where the highest peak is around $u/V \approx 5$ in figure 13(e), which corresponds to the large region of open flow in this particular sample, clearly seen in figure 9(e). In this case the pdf is bi-modal, with a second (lower) peak at $u/V \approx 2$ corresponding the the near-wall velocity.

For D170, shown in figure 13(a) and (b), the pdfs of both u/V and v/V are seen to broadly collapse onto a single curve for all Re, indicating that the normalised velocity distribution at the pore scale does not change with Re. Physically this can be interpreted as indicating that the preferred route the fluid takes through the porous sample is not different in the different flow regimes, which is reflected in figure 10. In contrast, in figures 13(c) for samples D430a there is a significant change in the pdf of u/V as the flow changes from the Darcy ($Re = 0.2$ and 3) to the transitional/turbulent ($Re = 19$ and 40) regimes. In figure 13(e) for D430b, there are small variations in the pdf for different Re, although the bi-modal shape is consistent and the variation cannot easily be explained by the different flow regimes. In figure 13(g and h) for D710, the distributions are similar for $Re = 5$ and 26 (before reaching turbulent regime) and change significantly through the transition to the turbulent regime ($Re = 57$ and 140) as non-dimensional velocities in the range $1 < u/V < 3$ become more common and the distribution of velocity is generally more uniform. This increased uniformity is very obviously visible in figure 11(d). In this sample there are some negative longitudinal velocities when the Reynolds number is high ($Re = 57$ and 140), which means there are locations where the velocity is to some extent opposing the bulk flow direction, i.e. there is reversed flow or recirculation. Indeed, a recirculation region was observed in the velocity contour map of D710 in figure 11 (marked with red circles). Unfortunately, this region is near the edge of our FOV so it is difficult to fully explain, however, it appears to be a result of the large obstruction caused by the glass sphere at the bottom of the FOV. The surrounding particles (out of FOV in three dimension) must force the fluid into taking this particularly tortuous route in order to navigate this obstacle. The fact that this only happens at the higher Reynolds numbers indicates the influence that inertia has on the possible flow paths. Negative values of the longitudinal velocity component are also found by Maier et al. [66] using Lattice-Boltzmann simulations and Kutsovsky et al. [67] using nuclear magnetic resonance imaging to study flow through packed beds. Their findings also indicate that the negative tails of the pdf decreases as the Reynolds number decreases, which is consistent with our results. Overall, the velocity distribution in the different flow regimes is well explained by the local geometry in our selected samples and it is not possible to make any general conclusions about the effect of particle size. In order to do this a much wider range of samples and measurement zones would be required for all particle sizes, which would be extremely time-consuming.
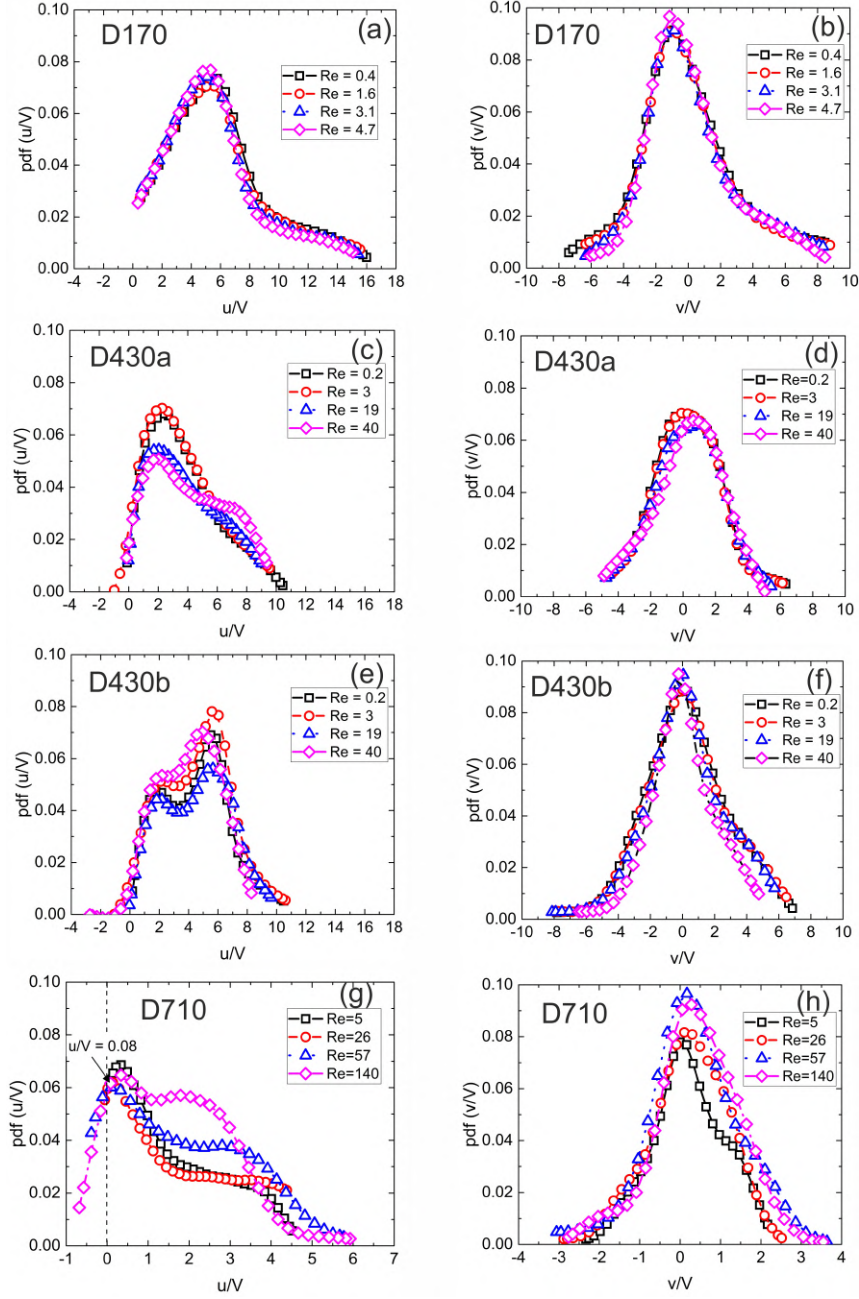
Figure 13: (a), (c), (e) and (g) are probability density functions (pdfs) of u/V for D170, D430a, D430b and D710, and (b), (d), (f) and (h) are the corresponding pdfs of v/V. Note that the abscissa in (g) and (h) for D710 are different to the others.

23

5. Velocity fluctuation at the pore scale

The distribution of velocity fluctuation intensity in the sintered glass samples was studied to better understand the flow behaviour at the pore scale. In arriving at these results, the local mean velocity components were subtracted from each instantaneous velocity record. The longitudinal velocity fluctuation and the local magnitude of the velocity fluctuation are presented and they are normalized by the Darcian velocity and the local time-averaged velocity respectively. Hence, the longitudinal velocity fluctuation is defined as $\sqrt{u'^2}/V$ and the local velocity fluctuation intensity is defined as $\sqrt{u'^2 + v'^2}/\bar{U}$, where u' and v' are fluctuations of each velocity component. The velocity fluctuations in D710 are presented in this section.

5.1. Longitudinal velocity fluctuation

Figure 14 shows the longitudinal velocity fluctuation normalised by Darcian velocity in D710. Overall, the longitudinal velocity fluctuation increases as Re increases, especially after entering the turbulent regime, and the fluctuation is unevenly distributed at the pore scale. The longitudinal velocity fluctuation distribution in the pre-Darcy ($Re = 5$) and Forchheimer ($Re = 26$) regimes is nearly identical in which the majority of the strong fluctuation are in the near wall region. There is some variation in the intensity of the fluctuations, which are generally higher in the Forchheimer regime (as expected) except for inside the region in the red dotted box. These results indicate that there are very large variations in local fluctuation intensity based on the local geometry even when the bulk flow is considered to be in the Darcy regime, as such the flow could be considered to be in different regimes at different locations in the same geometry. Given the large variation in the local mean velocity seen in §4.2 and the significant variation in the characteristic length of the plethora of flow passages, it would be expected to see large variations in the local Re if it were calculated based on local parameters. This further explains why the identification of flow regimes from bulk flow properties is often difficult and consistency across results of different geometries, porosities and types of media is so difficult to achieve.

The intensity of the velocity fluctuations becomes stronger in the near wall region in turbulent regime ($Re = 57$, 140) and the significant velocity fluctuations start to spread to regions further from the wall. However, it is still apparent that at all Re tested there are still some regions of relatively quiescent flow indicating that even at the highest Re we tested strong turbulent fluctuations have not spread throughout the entire geometry and still depend on the local geometry. Strong fluctuations are evident in the GHPQ region in figure 14(c) where the flow from inlets 1 and 2 meet. The fluctuations are particularly intense above the line linking P and Q, which implies that this unsteadiness is primarily coming from inlet 1 (the precise source is unclear). There is also a region of high fluctuation intensity at the wall near point P, particularly at $Re = 140$ in figure 14(d). This is the location of a stagnation point on the front face of the sphere. The large fluctuations are induced by small changes in the
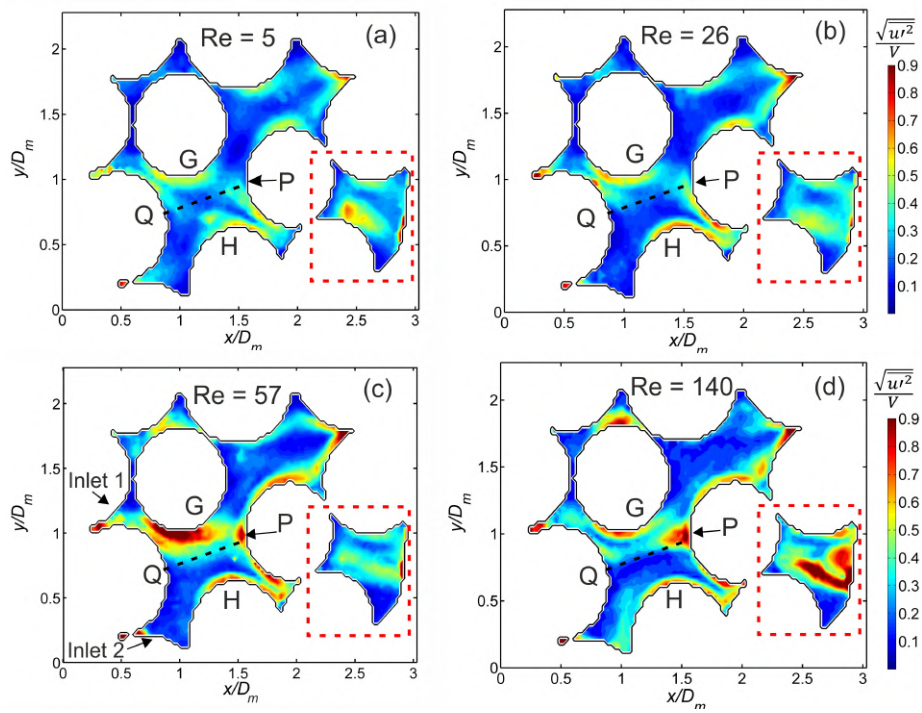
Figure 14: Contour plots of longitudinal velocity fluctuation normalised by Darcian velocity in the region D710 at (a) Re = 5, (b) Re = 26, (c) Re = 57 and (d) Re = 140.

exact location of this stagnation point as the upstream conditions (i.e. small variations in the competing flow through inlets 1 and 2) change in time.

Figure 14 also shows that the fluctuation intensity in the red rectangle (marked in the figure) is very strong in the turbulent regime (Re = 140) and it can be inferred that this is due to the flow from the z-direction (into or out of the focal plane) because there is no entry to this area in the focal plane. This demonstrates the difficulty of interpreting the flow patterns and fluctuations based only on local geometric features visible in the focal plane and highlights the strong three-dimensionality of the flow.

5.2. Local velocity fluctuation intensity

The local magnitude of the velocity fluctuations ($\sqrt{u'^2 + v'^2}/\bar{U}$) is a measure of the local fluctuation intensity and the closest proxy we can obtain for turbulence intensity with our two-dimensional results. This intensity is seen to be very large in the vicinity of all the walls throughout the FOV. This is not only because the fluctuations are high near the wall, but also that the mean velocity magnitude ($\bar{U}$), which is used to normalise the intensity, is small near the wall. (In addition the measurement uncertainty is also highest in the near-wall region due to reflections from the glass.) Figure 15 plots local velocity fluctuation intensity along the line GH in figure 14 at all the Reynolds numbers tested. It can be seen that in the near wall region (which we have indicatively labelled in figure 15) the fluctuation intensity is rather high at all Re for the reasons mentioned above. In the central region, however, we see a significant change with increasing Reynolds number, with a particular increase in intensity in the turbulent regimes. In the non-near wall region, the velocity fluctuation intensity is close to 5% in the Darcy and Forchheimer regimes and around 10% in the turbulent regime. (These numbers also include any measurement noise, which is estimated to be a few percent, see §2.)

As shown in previous work [56], transition between the Dary-Forchheimer and turbulent flow can be observed by examining the variation of the intensity of the velocity fluctuation with Re. Figure 16 shows the variation of velocity fluctuation intensity with Re in D710. Two values have been calculated, one for the whole two-dimensional FOV in which there is a reliably measureble flow, and the other across the line GH from figure 14, which was the subject of figure 15. The reduced pressure drop ($\Delta P/LV$) is presented on the same plot (left-hand y-axis) to compare the critical Reynolds number obtained from these two methods. The different flow regimes are marked with different colours according to the reduced pressure drop plots. Figure 16 shows that the transition regime obtained from the pressured drop measurement agrees well with that obtained from μ-PIV measurement of velocity fluctuation intensity. It demonstrates that the flow in the pre-Darcy, Darcy and Forchheimer regimes is laminar because the velocity fluctuation keeps at a approximately constant, relatively low value at Reynolds numbers below transiton, and increases dramatically after transition.
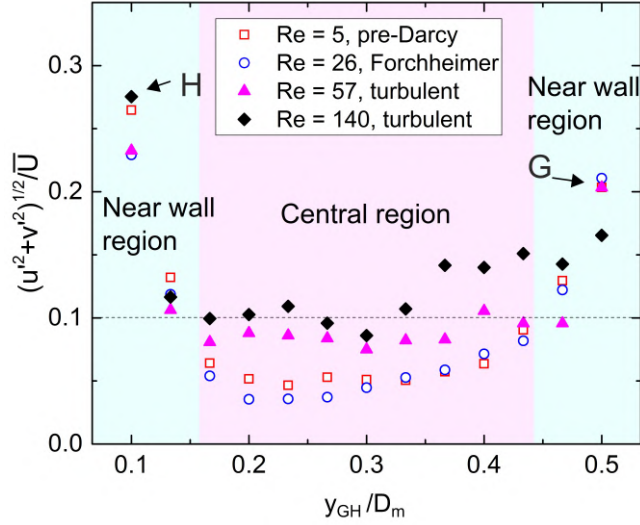
Figure 15: The time-averaged local velocity fluctuation intensity along the line GH in figure 14 at $Re =$5, 26, 57 and 140. The near wall region and central region are approximately indicated with different colours.
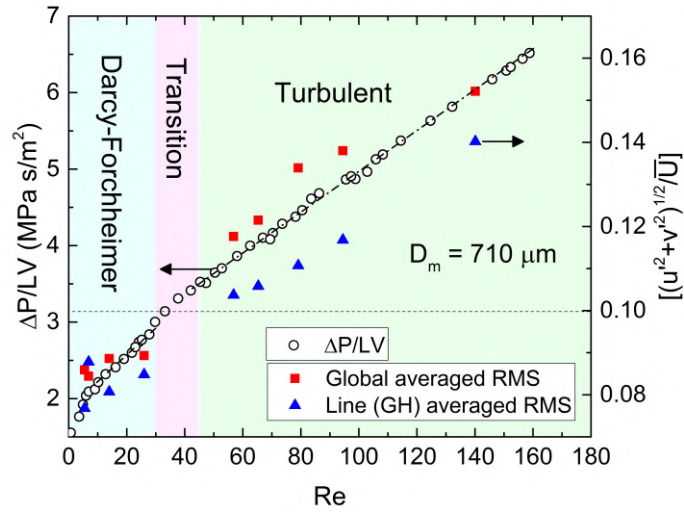

Figure 16: Velocity fluctuation intensity (right-hand y-axis) and reduced pressure drop (left-hand y-axis) versus Reynolds number for D710. Flow regimes are marked with different colours according to the pressure data.

6. Summary and conclusions

In this study, micro-scale sintered glass samples, with different mean sphere sizes (of D_m =170, 430 and 710 μm), were fabricated by slightly sintering glass spheres in a sandwich structure. The pressure drop over each of the whole sintered glass samples and flow visualization in four different locations within the samples were studied using pressure drop measurements and μ-PIV measurements respectively.

Pressure drop measurements enable the identification of the flow regimes usually associated with flow through the porous media. In the current study, four different flow regimes, identified as pre-Darcy, Darcy, Forchheimer and turbulent, were found as the Reynolds number was increased. It is found that the pressure drop depends strongly on particle size and shows a linear relationship with Reynolds number in the Darcy regime and a non-linear relationship in other regimes. It is also found that the permeability increases and the form drag coefficient decreases with increasing particle size due to the lower surface area impeding the flow path allowing for a less tortuous flow path. Neither the mean sphere diameter based Reynolds number nor the permeability based Reynolds number show perfect agreement with previous studies when comparing the corresponding flow regime boundaries. However, it is consistent that the onset Re of each flow regime increases with increasing porosity and particle size.

The μ-PIV results show that the velocity profiles through the channels within the porous media are often near-parabolic, especially in the Darcy and Forchheimer regimes. In the turbulent regime the effects of inertia are more often apparent in the formation of localised jets within the flow. However, examination of the velocity distribution at the pore scale shows that in some geometries, the flow remains largely the same in all the different flow regimes, whilst in other geometries significant differences can be observed between flow regimes. What is most evident is that the velocity distribution is highly dependent on the local geometric features and it is possible to observe localised large fluctuations within the pores even when the bulk flow through the sample is considered to be in the Darcy regime. In contrast, local regions of relatively quiescent flow can be observed when the bulk flow is considered to be in the turbulent regime, although the overall magnitude of the fluctuations throughout the whole geometry is shown to be a good indicator of the flow regime (or at least it is commensurate with the pressure drop measurements). However, it appears that even at the highest Re tested the flow is not really fully turbulent and will continue to develop with increasing Re. This phenomenon could be explained through a local Reynolds number as it is not uncommon to observe local velocities differing by a factor of ~ 10 within the same sample. However, these observations go some way to explaining why obtaining a consistent scaling for porous media has proved difficult and there are often discrepancies between different materials and geometries, particularly in determining the value of a critical Reynolds number.

Acknowledgments

References

[1] M. J. De Lemos, Turbulence in porous media: modeling and applications, Elsevier, 2012.

[2] A. Kasaeian, R. Daneshazarian, O. Mahian, L. Kolsi, A. J. Chamkha, S. Wongwises, I. Pop, Nanofluid flow and heat transfer in porous media: A review of the latest developments, Int. J. Heat and Mass Transfer 107 (2017) 778 – 791.

[3] D. T. Lin, J. C. Hsieh, B. Y. Shih, The optimization of geothermal extraction based on supercritical CO2 porous heat transfer model, Renewable Energy 143 (2019) 1162 – 1171.

[4] A. Izadi, M. Siavashi, H. Rasam, Q. Xiong, MHD enhanced nanofluid mediated heat transfer in porous metal for CPU cooling, Appl. Thermal Eng. 168.

[5] I. Medved, R. Ĉerný, Modeling of radionuclide transport in porous media: A review of recent studies, J. Nuclear Mats 526 (2019) 151765.

[6] H. Zeng, Y. Wang, S. Gong, Y. Shi, N. Cai, Catalytically enhanced methane-rich combustion by porous media reactor, Fuel 248 (2019) 65 – 75.

[7] L. J. Gibson, M. F. Ashby, Cellular solids: structure and properties, Cambridge university press, 1999.

[8] K. Diao, Z. Xiao, Y. Zhao, Specific surface areas of porous cu manufactured by lost carbonate sintering: Measurements by quantitative stereology and cyclic voltammetry, Materials Chemistry and Physics 162 (2015) 571–579.

[9] K. Diao, L. Zhang, Y. Zhao, Measurement of tortuosity of porous cu using a diffusion diaphragm cell, Measurement 110 (2017) 335–338.

[10] D. B. Ingham, I. Pop, Transport phenomena in porous media, Elsevier, 1998.

[11] A. Satter, G. M. Iqbal, Fundamentals of fluid flow through porous media, in: Reservoir Engineering, Gulf Professional Publishing, 2016, pp. 155 – 169.

[12] P. Venkataraman, P. R. M. Rao, Darcian, transitional, and turbulent flow through porous media, Journal of Hydraulic Engineering 124 (8) (1998) 840–846.

[13] H. Darcy, Les fontaines publiques de la ville de Dijon: exposition et application, Victor Dalmont, 1856.

[14] P. Forchheimer, Water movement through the ground., Zeitschrift des vereines deutscher ingenieure 45 (1901) 1781–1788.

[15] D. Hlushkou, U. Tallarek, Transition from creeping via viscous-inertial to turbulent flow in fixed beds, J. Chromatography A 1126 (1) (2006) 70 – 85.

[16] Z. Cheng, Z. Ning, Q. Wang, Y. Zeng, R. Qi, L. Huang, W. Zhang, The effect of pore structure on non-Darcy flow in porous media using the lattice Boltzmann method, J. Petroleum Sci. and Eng. 172 (2019) 391 – 400.

[17] M. I. Miah, M. A. Elhaj, S. Ahmed, M. E. Hossain, Modeling of temperature distribution and oil displacement during thermal recovery in porous media: A critical review, Fuel 226 (2018) 423 – 440.

[18] M. J. Blunt, Flow in porous media – pore-network models and multiphase flow, Current Opinion in Colloid and Interface Science 6 (3) (2001) 197 – 207.

[19] A. Dybbs, R. Edwards, A new look at porous media fluid mechanicsdarcy to turbulent, in: Fundamentals of transport phenomena in porous media, Springer, 1984, pp. 199–256.

[20] R. Fand, B. Kim, A. Lam, R. Phan, Resistance to the flow of fluids through simple and complex porous media whose matrices are composed of randomly packed spheres, J. Fluids Eng 109 (3) (1987) 268–274.

[21] I. Kececioglu, Y. Jiang, Flow through porous media of packed spheres saturated with water, J. Fluids Eng 116 (1) (1994) 164–170.

[22] P. Kundu, V. Kumar, I. M. Mishra, Experimental and numerical investigation of fluid flow hydrodynamics in porous media: Characterization of pre-Darcy, Darcy and non-Darcy flow regimes, Powder Technology 303 (2016) 278 – 291.

[23] Z. Li, J. Wan, K. Huang, W. Chang, Y. He, Effects of particle diameter on flow characteristics in sand columns, Int. J. Heat and Mass Transfer 104 (2017) 533 – 536.

[24] J. H. van Lopik, R. Snoeijers, T. C. G. W. van Dooren, A. Raoof, R. J. Schotting, The Effect of Grain Size Distribution on Nonlinear Flow Behavior in Sandy Porous Media, Transport in Porous Media 120 (1) (2017) 37–66.

[25] B. P. Muljadi, M. J. Blunt, A. Q. Raeini, B. Bijeljic, The impact of porous media heterogeneity on non-Darcy flow behaviour from pore-scale simulation, Advances in Water Resources 95 (2016) 329 – 340.

[26] M. Fourar, G. Radilla, R. Lenormand, C. Moyne, On the non-linear behavior of a laminar single-phase flow through two and three-dimensional porous media, Adv. in Water Resources 27 (6) (2004) 669 – 677.

[27] M. S. Newman, X. Yin, Lattice Boltzmann simulation of non-Darcy flow in stochastically generated 2D porous media geometries, SPE Journal 18 (1) (2013) 12–26.

[28] D. Chiappini, G. Bella, A. Festuccia, A. Simoncini, Direct numerical simulation of an open-cell metallic foam through lattice Boltzmann method, Communications in Computational Physics 18 (3) (2015) 707–722.

[29] M. Cloete, G. Smit, M. Maritz, External boundary effects on the velocity profile for generalized Newtonian fluid flow inside a homogeneous porous medium, J. Non-Newtonian Fluid Mech. 215 (2015) 40 – 52.

[30] M. Sheikholeslami, New computational approach for exergy and entropy analysis of nanofluid under the impact of Lorentz force through a porous media, Computer Methods in Applied Mechanics and Engineering 344 (2019) 319 – 333.

[31] M. S. Astanina, M. A. Sheremet, H. F. Oztop, N. Abu-Hamdeh, MHD natural convection and entropy generation of ferrofluid in an open trapezoidal cavity partially filled with a porous medium, Int. J. Mech. Sci. 136 (2018) 493 – 502.

[32] N. S. Gibanov, M. A. Sheremet, H. F. Oztop, N. Abu-Hamdeh, Effect of uniform inclined magnetic field on mixed convection in a lid-driven cavity having a horizontal porous layer saturated with a ferrofluid, Int. J. Heat and Mass Transfer 114 (2017) 1086–1097.

[33] W. Johnston, A. Dybbs, R. Edwards, Measurement of fluid velocity inside porous media with a laser anemometer, The Physics of fluids 18 (7) (1975) 913–914.

[34] A. Yarlagadda, A. Yoganathan, Experimental studies of model porous media fluid dynamics, Experiments in Fluids 8 (1-2) (1989) 59–71.

[35] T. Kyoden, S. Akiguchi, T. Tajiri, T. Andoh, N. Furuichi, R. Doihara, T. Hachiga, Assessing the infinitely expanding intersection region for the development of large-scale multipoint laser Doppler velocimetry, Flow Measurement and Instrumentation 70.

[36] F. Ingegnoli, N. Ughi, G. Dinsdale, A. Orenti, P. Boracchi, Y. Allanore, I. Foeldvari, A. Sulli, M. Cutolo, V. Smith, A. L. Herrick, EULAR Study Grp Microcirculati, An international SUrvey on non-iNvaSive tecHniques

to assess the mIcrocirculation in patients with RayNaud's phEnomenon (SUNSHINE survey), Rheumatology Int. 37 (11) (2017) 1879–1890.

[37] A. Sederman, M. Johns, A. Bramley, P. Alexander, L. Gladden, Magnetic resonance imaging of liquid flow and pore structure within packed beds, Chemical Engineering Science 52 (14) (1997) 2239–2250.

[38] T. Baumann, C. J. Werth, Visualization of colloid transport through heterogeneous porous media using magnetic resonance imaging, Colloids and surfaces A: Physicochemical and engineering aspects 265 (1-3) (2005) 2–10.

[39] A. Fheed, K. Kodowski, A. Krzyak, Fracture orientation and fluid flow direction recognition in carbonates using diffusion-weighted nuclear magnetic resonance imaging: An example from Permian, J. Appl. Geophysics 174 (2020) 103964.

[40] L. Jiang, Y. Song, Y. Liu, M. Yang, N. Zhu, T. Wang, Y. Zhao, Magnetic resonance imaging of CO_2/water two phase flow in porous media, Energy Procedia 37 (2013) 6839 – 6845.

[41] S. Saleh, J. Thovert, P. Adler, Measurement of two-dimensional velocity fields in porous media by particle image displacement velocimetry, Experiments in Fluids 12 (3) (1992) 210–212.

[42] M. Rashidi, L. Peurrung, A. Tompson, T. Kulp, Experimental analysis of pore-scale flow and transport in porous media, Advances in Water Resources 19 (3) (1996) 163–180.

[43] Y. A. Hassan, E. Dominguez-Ontiveros, Flow visualization in a pebble bed reactor experiment using piv and refractive index matching techniques, Nuclear Engineering and Design 238 (11) (2008) 3080–3085.

[44] A. Y. Huang, M. Y. Huang, H. Capart, R.-H. Chen, Optical measurements of pore geometry and fluid velocity in a bed of irregularly packed spheres, Experiments in Fluids 45 (2) (2008) 309–321.

[45] S. Fu, P. H. Biwole, C. Mathis, Particle tracking velocimetry for indoor airflow field: A review, Building and Environment 87 (2015) 34–44.

[46] F. Tauro, R. Piscopia, S. Grimaldi, PTV-Stream: A simplified particle tracking velocimetry framework for stream surface flow monitoring, CATENA 172 (2019) 378–386.

[47] L. Sarno, A. Carravetta, Y.-C. Tai, R. Martino, M. Papa, C.-Y. Kuo, Measuring the velocity fields of granular flows - employment of a multi-pass two-dimensional particle image velocimetry (2D-PIV) approach, Advanced Powder Technology 29 (12) (2018) 3107–3123.

[48] X. Wen, Y. Liu, H. Tang, Unsteady behavior of a sweeping impinging jet: Time-resolved particle image velocimetry measurements, Exp. Thermal and Fluid Sci. 96 (2018) 111–127.

[49] N. Horton, D. Pokrajac, Onset of turbulence in a regular porous medium: An experimental study, Physics of fluids 21 (4) (2009) 045104.

[50] R. Lima, S. Wada, S. Tanaka, M. Takeda, T. Ishikawa, K. Tsubota, Y. Imai, T. Yamaguchi, In vitro blood flow in a rectangular PDMS microchannel: experimental observations using a confocal micro-PIV system, Biomedical Microdevices 10 (2) (2008) 153–167.

[51] R. Lima, S. Wada, K. Tsubota, T. Yamaguchi, Confocal micro-PIV measurements of three-dimensional profiles of cell suspension flow in a square microchannel, Meas. Sci. and Tech. 17 (4) (2006) 797–808.

[52] C. Pan, H. Chuang, C. Cheng, C. Yang, Micro-flow measurement with a laser diode micro-particle image velocimetry, Sensors and Actuators A: Physical 116 (1) (2004) 51–58.

[53] S. Roman, C. Soulaine, M. A. AlSaud, A. Kovscek, H. Tchelepi, Particle velocimetry analysis of immiscible two-phase flow in micromodels, Advances in Water Resources 95 (2016) 199–211.

[54] A. C. Marin, T. Grossi, E. Bianchi, G. Dubini, D. Lacroix, μ-particle tracking velocimetry and computational fluid dynamics study of cell seeding within a 3D porous scaffold, J. Mechanical Behavior of Biomedical Materials 75 (2017) 463–469.

[55] M. Heshmati, M. Piri, Interfacial boundary conditions and residual trapping: A pore-scale investigation of the effects of wetting phase flow rate and viscosity using micro-particle image velocimetry, Fuel 224 (2018) 560–578.

[56] X. Lu, Y. Zhao, D. J. C. Dennis, Flow measurements in microporous media using micro-particle image velocimetry, Phys. Rev. Fluids 3 (2018) 104202.

[57] D. Wang, L.-S. Fan, Particle characterization and behavior relevant to fluidized bed combustion and gasification systems, in: Fluidized bed technologies for near-zero emission combustion and gasification, Elsevier, 2013, pp. 44–46.

[58] V. A. Patil, J. A. Liburdy, Flow characterization using piv measurements in a low aspect ratio randomly packed porous bed, Experiments in fluids 54 (4) (2013) 1497.

[59] V. A. Patil, J. A. Liburdy, Optical measurement uncertainties due to refractive index mismatch for flow in porous media, Experiments in fluids 53 (5) (2012) 1453–1468.

[60] H. W. Coleman, W. G. Steele, Experimentation, validation, and uncertainty analysis for engineers, John Wiley & Sons, 2018.

[61] C. D. Meinhart, S. T. Wereley, J. G. Santiago, Piv measurements of a microchannel flow, Experiments in fluids 27 (5) (1999) 414–419.

[62] P. I. Polubarinova-Koch, Theory of ground water movement, Princeton University Press, 2015.

[63] I. Macdonald, M. El-Sayed, K. Mow, F. Dullien, Flow through porous media-the ergun equation revisited, Industrial & Engineering Chemistry Fundamentals 18 (3) (1979) 199–208.

[64] S. S. Datta, H. Chiang, T. Ramakrishnan, D. A. Weitz, Spatial fluctuations of fluid velocities in flow through a three-dimensional porous medium, Physical Review Letters 111 (6) (2013) 064501.

[65] D. Sen, D. S. Nobes, S. K. Mitra, Optical measurement of pore scale velocity field inside microporous media, Microfluidics and nanofluidics 12 (1-4) (2012) 189–200.

[66] R. S. Maier, D. Kroll, Y. Kutsovsky, H. Davis, R. S. Bernard, Simulation of flow through bead packs using the lattice boltzmann method, Physics of Fluids 10 (1) (1998) 60–74.

[67] Y. Kutsovsky, L. Scriven, H. Davis, B. Hammer, Nmr imaging of velocity profiles and velocity distributions in bead packs, Physics of Fluids 8 (4) (1996) 863–871.